ACCSCIENCE PUBLISHING

International Journal of Bioprinting

RESEARCH ARTICLE

Fabrication of an *in vitro* three-dimensional tumor model using liver-derived decellularized extracellular matrix/gelatin methacrylate bioink for investigating cancer characteristics and drug resistance

Chunyang Zhang[1,2†], Yunze Xu[1,2†], Hongwei Yu[1,2], Xiaochang Lu[1,3], Ying Fang[1,2], Changyong Li[1,3], Weihong Ji[1,3], Shibin Wang[1,2], Aizheng Chen[1,3], and Chaoping Fu[1,2*]

[1]Institute of Biomaterials and Tissue Engineering & Fujian Provincial Key Laboratory of Biochemical Technology, Huaqiao University, Xiamen, Fujian, China

[2]College of Materials Science and Engineering, Huaqiao University, Xiamen, Fujian, China

[3]College of Chemical Engineering, Huaqiao University, Xiamen, Fujian, China

(This article belongs to the *Special Issue*: *Advanced Strategies in 3D Bioprinting for Disease Modelling*)

Abstract

Three-dimensional (3D) printing has emerged as a promising technique for creating *in vitro* tumor models that replicate the tumor microenvironment, with the potential to reduce or replace the use of experimental animals. The incorporation of 3D decellularized extracellular matrix (dECM) hydrogels significantly enhances cellular responsiveness and functionality in drug screening. However, the limited printability of dECM restricts its application in e*x vivo* 3D disease models. To address this limitation, researchers have developed a blended bioink composed of dECM, gelatin methacrylate (GelMA), and gelatin, specifically tailored for direct ink writing-based 3D bioprinting. This formulation exhibits favorable shear-thinning behavior, enhanced viscosity, and thermal-sensitive properties, making it suitable for 3D bioprinting. The combination of dECM with GelMA and gelatin not only improves the printability of the bioink but also enhances the resolution of the printed scaffolds. Furthermore, dECM demonstrated positive effects on human hepatocellular carcinoma (HepG2) cells, promoting proliferation, migration, and cell spheroid formation. A 3D liver cancer model was successfully created *in vitro* by printing HepG2 cells encapsulated in the bioink containing dECM. This model exhibited characteristics akin to *in vivo* solid tumors, including notable cell proliferation, protein secretion, and substantial cell spheroid formation (up to 78.83 ± 9.41 μm on day 8). Additionally, it showed drug resistance, with 46.23% and 31.34% cell viability observed at 100 μg/mL concentrations of doxorubicin and paclitaxel, respectively. These findings underscore the potential of bioprinted 3D tumor models composed of GelMA, gelatin, and dECM as valuable platforms for the evaluation of anticancer drugs.

Keywords: 3D tumor model; Decellularized extracellular matrix; Drug evaluation; Gelatin methacrylate; Printability

†These authors contributed equally to this work.

***Corresponding author:**
Chaoping Fu
(fuchp@hqu.edu.cn)

Citation: Zhang C, Xu Y, Yu H, *et al*. Fabrication of an *in vitro* three-dimensional tumor model using liver-derived decellularized extracellular matrix/gelatin methacrylate bioink for investigating cancer characteristics and drug resistance. *Int J Bioprint*. 2025;11(4):392-408. doi: 10.36922/IJB025160142

Received: April 14, 2025
Revised: May 24, 2025
Accepted: June 9, 2025
Published online: June 10, 2025

1. Introduction

Cancer is a pervasive global public health challenge, significantly impacting human life and well-being. In recent years, effective treatments for cancer include surgical resection,[1,2] radiotherapy,[3,4] and chemotherapy.[5,6] Nevertheless, the 5-year survival rate of patients remains suboptimal. On one hand, current treatments fail to achieve a complete cure. On the other hand, our understanding of the complex mechanisms and characteristics of tumors remains incomplete, hindering the development of effective therapies and drugs.[7,8] Currently, preclinical research on anticancer drugs heavily relies on two-dimensional (2D) cell and animal models. However, the simplicity of 2D cell models and the limitations of animal experiments, such as long timelines, limited reproducibility, and high costs, hinder the development of effective tumor treatments.[9–11] Thus, there is an urgent need for sophisticated models that accurately simulate three-dimensional (3D) solid tumors *in vivo*. Such models hold great promise for facilitating more comprehensive tumor research, improving pharmacological evaluations, and accelerating drug development.

The emergence of 3D cell culture technology has revolutionized the advancement of *in vitro* tumor models. Within a 3D culture system, the establishment of an extracellular matrix (ECM) and the incorporation of diverse signals that mimic the growth characteristics of tumor cells are of utmost importance.[12–15] Through the implementation of 3D culture, tumor models can be meticulously crafted by manipulating the properties of the matrix or scaffold, thereby facilitating the investigation of morphogenesis, angiogenesis, invasion, pharmacology, and other tumor-related attributes.[16,17] Consequently, 3D bioprinting emerges as a promising approach for the construction of standardized 3D tumor models. By harnessing the capabilities of 3D printing technology, bioprinting enables the seamless integration of cells and biological materials, layer by layer, resulting in the generation of tissue-like structures.[18,19]

Natural hydrogels like fibrinogen, cellulose, chitosan, alginate, and hyaluronic acid are extensively used as bioinks in bioprinting for their controllable mechanical properties and excellent biocompatibility.[20–23] Bioprinting significantly enhances the reproducibility and standardization of 3D tumor models, making it ideal for preclinical research.[24,25] 3D-bioprinted tissues help reduce model variability, improve the consistency and reliability of drug screening data, and lower the risk and cost of drug screening.[26–28] However, establishing a tumor model relies on critical cellular, biochemical, and mechanobiological cues. Although both natural and synthetic polymers have been used, they cannot fully replicate the complex ECM *in vivo*, which is a crucial microenvironment for cells.[29] The ECM is a complex and dynamic network that provides essential structural support and significantly influences various cellular functions,[30–33] including proliferation,[34] migration,[35] differentiation,[36,37] and signal transduction.[38,39] Consequently, accurately simulating or reconstructing the ECM *in vitro* is critical for developing tumor models that closely mimic physiological conditions.[40,41]

Decellularization technology offers a promising method to selectively eliminate cellular components from tissues or organs while retaining the essential ECM components, biological functions, and structural integrity. This advanced technique has significantly broadened the use of ECM materials in the biomedical field.[42,43] However, decellularized ECM (dECM)-based bioinks suffer from suboptimal printability due to inadequate mechanical properties, unstable thermo-responsive behavior, and variable rheological properties, which limit their broader application in 3D bioprinting.[44,45]

In this study, we aimed to tackle the challenges posed by the limited printability of dECM-based bioinks while also developing an optimized bioink derived from liver tissue that demonstrates superior 3D printability. Our formulation not only improved printability but also exhibited excellent biocompatibility and favorable interactions with HepG2 cells, a liver cancer cell line. To comprehensively evaluate the physical and biological attributes of our bioink, we conducted a series of assessments encompassing morphology analysis, rheological characterization, degradation evaluation, swelling behavior analysis, 3D printability testing, and cytotoxicity analysis.

2. Materials and methods

2.1. Materials

Gelatin, methacrylic anhydride, sodium dodecyl sulfate, and ciprofloxacin were purchased from Aladdin Reagent Co., Ltd. (China). The porcine liver was procured from Mankouxiang Ecological Farming Cooperative Co., Ltd. (China). Cell Counting Kit (CCK)-8 and Dulbecco's Modified Eagle Medium were obtained from Keygen Biotech Corp., Ltd. (China). The bicinchoninic acid kit was purchased from Shanghai Biyuntian Biotechnology Co., Ltd. (China). The DNA kit was obtained from Cwbio, China; the glycosaminoglycan (GAG) kit from Genmed, China; and the collagen kit from Chondrex, United States of America (USA). Paclitaxel (PTX) and doxorubicin (DOX) were purchased from Solarbio Science and Technology Co., Ltd. (China). Calcein-acetoxymethyl/propidium iodide and acridine orange/ethidium bromide reagent kits were obtained from Solarbio Science and Technology Co., Ltd. (China).

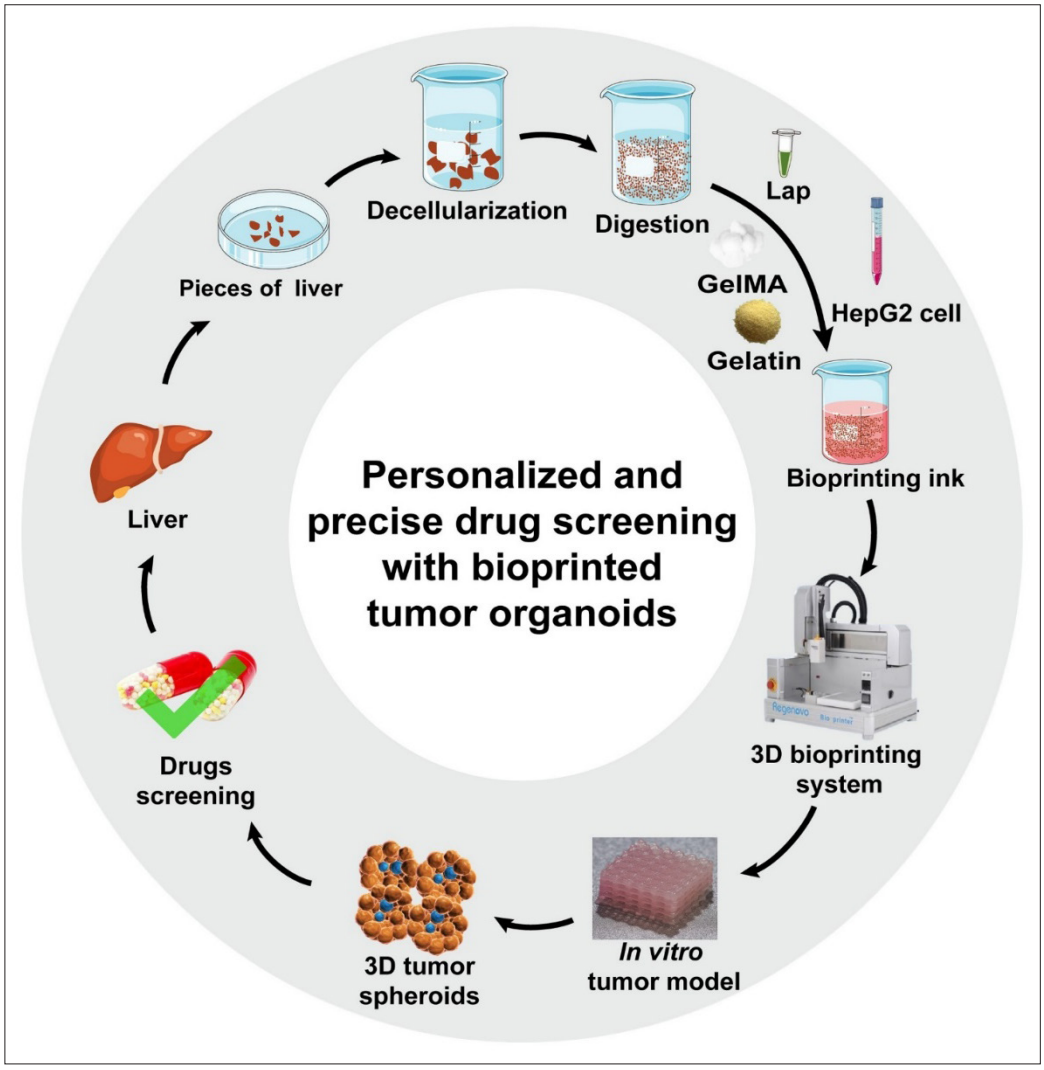

Schematic 1. Schematic diagram of the technological approach for this research. Abbreviations: GelMA, gelatin methacrylate; HepG2, human hepatocellular carcinoma; LAP, lithium phenyl-2,4,6-trimethylbenzoylphosphinate; 3D, three-dimensional.

2.2. Preparation and characterization of gelatin methacrylate and decellularized extracellular matrix

Initially, 10 g of gelatin was dissolved in 100 mL of phosphate-buffered saline (PBS) at 60°C, followed by the slow addition of 3 mL of methacrylic anhydride and stirring at 50°C for 3 h. The reaction was terminated by the addition of 500 mL of PBS. The resulting mixture was dialyzed against deionized water for 3 days (molecular weight: 12–14 kDa). After dialysis, the solution was filtered through a 0.22 μm membrane, and the filtrate was collected, pre-frozen at –80°C, then freeze-dried for 2 days and stored at –20°C in a sealed container. Finally, 20 mg of gelatin methacrylate (GelMA) sample was dissolved in 1 mL of deuterium oxide for proton nuclear magnetic resonance analysis to verify the synthesis. The Fourier-transform infrared (FTIR) spectra of freeze-dried GelMA were obtained using a NICOLET iS50 (Thermo Fisher Scientific, USA) equipped with a diamond attenuated total reflection module, analyzing the functional groups within the wavenumber range of 4000–500 cm^{-1}. Thermogravimetric analysis was conducted to investigate the thermal weight loss behavior of gelatin and GelMA (~10 mg). The analysis was performed under a nitrogen atmosphere, with a gas flow rate of 50 mL/min and a heating rate of 10°C/min, up to a final temperature of 500°C.

The preparation of dECM was carried out by combining chemical detergent and enzymatic treatment. Initially, 500 g wet liver tissue samples were cut into 10 × 10 mm^2 pieces and cleaned with ultrapure water for 30 min. Subsequently, the samples were treated with a 1% sodium dodecyl sulfate

solution for 14 h, followed by treatment with a DNase solution of 100 U/mL for 6 h, and washed with sterile PBS for 3 days, with 5 mg ciprofloxacin added to prevent bacterial contamination. The resulting decellularized liver matrix (DLM) was collected, washed with sterile PBS, freeze-dried, and stored at –20°C overnight. After 72 h of freeze-drying, the DLM was then digested in a solution of hydrochloric acid and pepsin. The digestion process took place at 37°C and 250 rpm for 6 h. The pepsin concentration was maintained at 1 mg/mL, with a hydrochloric acid concentration of 0.1 M and a ratio of 1:10 between the weight of DLM and the amount of pepsin used. After digestion, the pH was adjusted to neutral using a sodium hydroxide solution. The digested mixture was then subjected to dialysis with a 1000 D cutoff membrane for 3 days, with water replenished every 4 h. Finally, the dialyzed dECM was collected and freeze-dried for further use.

Both native liver tissues and DLM were immersed in a 4% paraformaldehyde solution for 24 h to fix the tissues. Following fixation, the tissues were embedded in the paraffin. Paraffined sections were cut into thin slices of 5 μm for deparaffinization and rehydration. Cell component residues were then observed by hematoxylin and eosin staining. In addition, 5-μm-thick sections of native and decellularized liver tissues were stained using the nuclear stain, 4',6-diamidino-2-phenylindole. The staining process was performed at room temperature for 5 min. Collagen I and III were also observed by immunohistochemical staining of tissue collagen.

For DNA, protein, collagen, GAG content, and proteomic analysis of dECM, a Tissue DNA extraction kit (Sigma-Aldrich, USA) was used to determine DNA content, a hydroxyproline assay kit (Aladdin Biotechnology Co., China) was employed to measure collagen content, and a GAG enzyme-linked immunosorbent assay kit (Sinopharm Chemical Reagent Co., China) was used to assess GAG content as an indicator of residual cells in dECM. A microplate reader (Thermo Scientific™ Multiskan™ GO, USA) was used to quantify the DNA, GAG, and collagen content.

2.3. Preparation of three-dimensional printing bioinks and characterization

Five different printing bioinks were prepared with varying compositions and ratios as follows: (i) 10% (w/v) GelMA (GM); (ii) 10% (w/v) GelMA and 5% (w/v) gelatin (GM/G); and (iii–v) GM/G combined with dECM at concentrations of 1%, 3%, and 5% (w/v), labeled as GM/G/d-1, GM/G/d-3, and GM/G/d-5, respectively. The components were dissolved in a PBS solution containing 0.25% (w/v) lithium phenyl-2,4,6-trimethylbenzoylphosphinate.

For morphology characterization, the bioinks with different ratios were cross-linked using ultraviolet (UV) light and subsequently immersed in PBS for 12 h to reach swelling equilibrium. After freeze-drying, the samples were fractured at the midpoint and coated with gold for 60 s using a conductive gel to secure them onto the holder. The fracture surface morphology of the hydrogels was then observed using scanning electron microscopy (SEM). Additionally, the internal pore sizes of the hydrogels were quantitatively analyzed using the Nano Measure software.

For rheological measurements, all tests were conducted using a rotational parallel plate rheometer (MCR 302, Anton Paar, Austria). A volume of 5 mL of each bioink was pipetted onto the bottom plate of the stage, with the gap distance set to 1 mm. Shear rate sweeps were conducted in the range of 0.1–800 s^{-1} at room temperature. Temperature–viscosity measurements were performed from 40 to 15°C. The storage modulus (*G'*) and loss modulus (*G"*) of the bioinks were evaluated by changing the temperature from 40 to 5°C, with a cooling rate of 5°C/min.

2.4. Three-dimensional printing

To bring the bioink to a pre-gel state, it was placed at 4°C for 20 min. Subsequently, the bioink cartridges were loaded into a 3D bioprinter, with the nozzle temperature set to 25°C and the print platform maintained at 4°C. During the printing process, the extrusion pressure was set to 0.25 MPa and the fill spacing was 1.2 mm. A porous scaffold with dimensions of 20 mm × 20 mm × 3 mm (length × width × height) was printed. After extrusion, the printed porous scaffold was exposed to UV light at an intensity of 30 mW/cm^2 for 30 s to induce cross-linking. To evaluate the printability of the bioink and the print resolution of the porous scaffold, the scaffold's surface morphology was analyzed using SEM, and the Pr value[44] was calculated. This value was determined based on the circularity of an enclosed area, as shown in **Equation (I)**:

$$c = 4\Pi A/L\text{^}2 \quad \text{(I)}$$

where c is circularity, L is the perimeter, and A is the area. A perfect circle yields a value of 1. For square shapes, the maximum circularity value is π/4. Therefore, the Pr parameter for square shapes can be calculated using **Equation (II)**:

$$Pr = \Pi / 4C\,L^2 / 16A \quad \text{(II)}$$

To measure the swelling ability of scaffolds, the freeze-dried scaffolds were first weighed and recorded as *Wd*. The scaffolds were then immersed in PBS (pH 7.4) at

room temperature, and their mass wet weight (*Ws*) was measured at 0, 2, 4, 6, and 12 h. The water swelling ratio (*Sr*) was calculated as a percentage using the following formula (**Equation III**):

$$Sr = (Ws - Wd)/Wd \times 100\% \quad \text{(III)}$$

To evaluate the degradation behavior of the composite porous scaffold, it was first subjected to swelling equilibrium, then freeze-dried and accurately weighed. Subsequently, the scaffold was immersed in a culture medium and incubated in a 37°C cell culture incubator. After 3, 6, and 9 days, the scaffold was retrieved, freeze-dried again, and its mass was recorded. The degradation rate of the hydrogel was calculated using the following formula (**Equation IV**):

$$D = (Wc - Wd)/Wc \times 100\% \quad \text{(IV)}$$

Cell cytotoxicity of printed scaffolds was assessed using L929 cells. The cells were cultured in Roswell Park Memorial Institute (RPMI) medium and maintained at 37°C with 100% humidity and 5% carbon dioxide. The cells were passaged every 2 days. The cytotoxicity of the scaffolds was assessed by extract assay. Briefly, using the culture medium as an extraction solvent, the freeze-dried scaffolds were soaked at a ratio of 0.2 g/mL for 24 h. A cell density of 8×10^3 was seeded into each well, and 100 μL of the corresponding scaffold extract was added. Three replicates were set for each group. After 24 and 48 h of culture, CCK-8 was added and viability was a 2-h incubation; the absorbance at 562 nm was measured to calculate cell viability. Similarly, live/dead staining was performed using calcein-acetoxymethyl/propidium iodide staining, where green indicates live cells and red indicates dead cells, to observe cell growth.

2.5. Three-dimensional *in vitro* tumor model construction

Human hepatocellular carcinoma (HepG2) cells were cultured in five types of gels at a density of 6×10^4 cells/mL and were crosslinked for 30 s with a 405 nm UV light. An appropriate medium was added to wash the scaffold, and the liquid culture was then changed. After 1, 2, and 3 days of culture, the absorbance was measured using the CCK-8 method. Simultaneously, the effect of the above hydrogels on HepG2 migration was determined using scratch assays. First, approximately 1×10^6 cells were seeded onto a six-well plate and incubated until they attained 80% confluence. A sterile 200 μL pipette tip was used to scratch the cell monolayer across the center, creating a cross-shaped wound in each well. Then, 500 μL of the hydrogel precursors were added to each scratch well. Images of the cells were captured at 0, 12, and 24 h using an Olympus microscope ($n = 3$). Finally, quantitative analysis was performed using Image J software (National Institutes of Health, Germany).

Liver-derived GelMA/dECM bioinks were utilized to fabricate an *in vitro* 3D liver cancer tumor model. Briefly, HepG2 cells were collected by centrifugation and suspended in the bioinks at a density of 1×10^6 cells/mL. The 3D printing procedure was performed as described previously. Finally, the bioprinted scaffold was transferred to a six-well plate, rinsed with PBS, and incubated in the culture medium.

To assess the cell viability of the tumor model, 3D scaffolds (3D control and 3D-dECM) cultured for 2, 4, 6, and 8 days, along with 2D cultured cells, were removed and washed twice with PBS to remove the culture medium. The cell proliferation was analyzed using CCK-8 for both 2D and 3D cultures. Meanwhile, live/dead staining was used to assess the survival state of cells.

For cell morphology, the sizes of tumor spheroids were monitored during 3D culture, with photographs taken for 2, 4, 6, and 8 days using an optical microscope. The sizes of tumor spheroids were quantified using Image J software (National Institutes of Health, Germany). Cells cultured in 2D were observed using phalloidin staining.

To assess liver function, culture supernatants were collected on day 8, and parameters including alanine aminotransferase (ALT), aspartate aminotransferase (AST), albumin (ALB), and total bile acid (TBA) were analyzed using a multimode microplate reader.

2.6. Chemosensitivity assay

The chemosensitivity of the 3D and 2D culture samples was assessed by treating them with various concentrations of different drugs. After 6 days of cultivation, the samples were treated with PTX and amrubicin hydrochloride. Specifically, PTX was dissolved in 0.1% dimethyl sulfoxide and diluted with the culture medium, while amrubicin hydrochloride was dissolved in ultrapure water and similarly diluted. The drug concentrations used were 10, 20, 30, 50, 100, and 200 μg/mL. Each well was filled with the corresponding drug concentration, and cell viability and survival rate were measured using the CCK-8 assay after 12 and 24 h. Live/dead staining was performed simultaneously to assess cell survival.

2.7. Statistical analysis

At least three independent experiments were performed, unless otherwise stated. One-way analysis of variance and *t*-tests were used to analyze the differences between the

experimental groups. Statistical significance was indicated as follows: * $p < 0.05$, ** $p < 0.01$, *** $p < 0.001$.

3. Results and discussion

3.1. Gelatin methacrylate and liver decellularized extracellular matrix preparation and characterization

In this experiment, chemical and enzymatic treatments were employed for decellularization, as illustrated in Figure 1A. After decellularization, the liver tissue became translucent, indicating the effective removal of cellular components. The resulting dECM was lyophilized into a white powder. To evaluate the efficacy of decellularization, quantitative analysis of DNA and main biological components, histological staining, and morphological analysis were performed. Figure 1B depicts the results of hematoxylin and eosin and 4',6-diamidino-2-phenylindole staining, which clearly demonstrate the absence of cellular components in DLM. SEM images revealed a porous layered fiber structure in the decellularized tissue. Morphological observations of the dECM powder confirmed that the hydrochloric acid and pepsin mixture successfully digested the DLM into particles averaging approximately 700 μm in size (Figure 1C). Figure 1D illustrates the content of biological components, with DNA levels decreasing

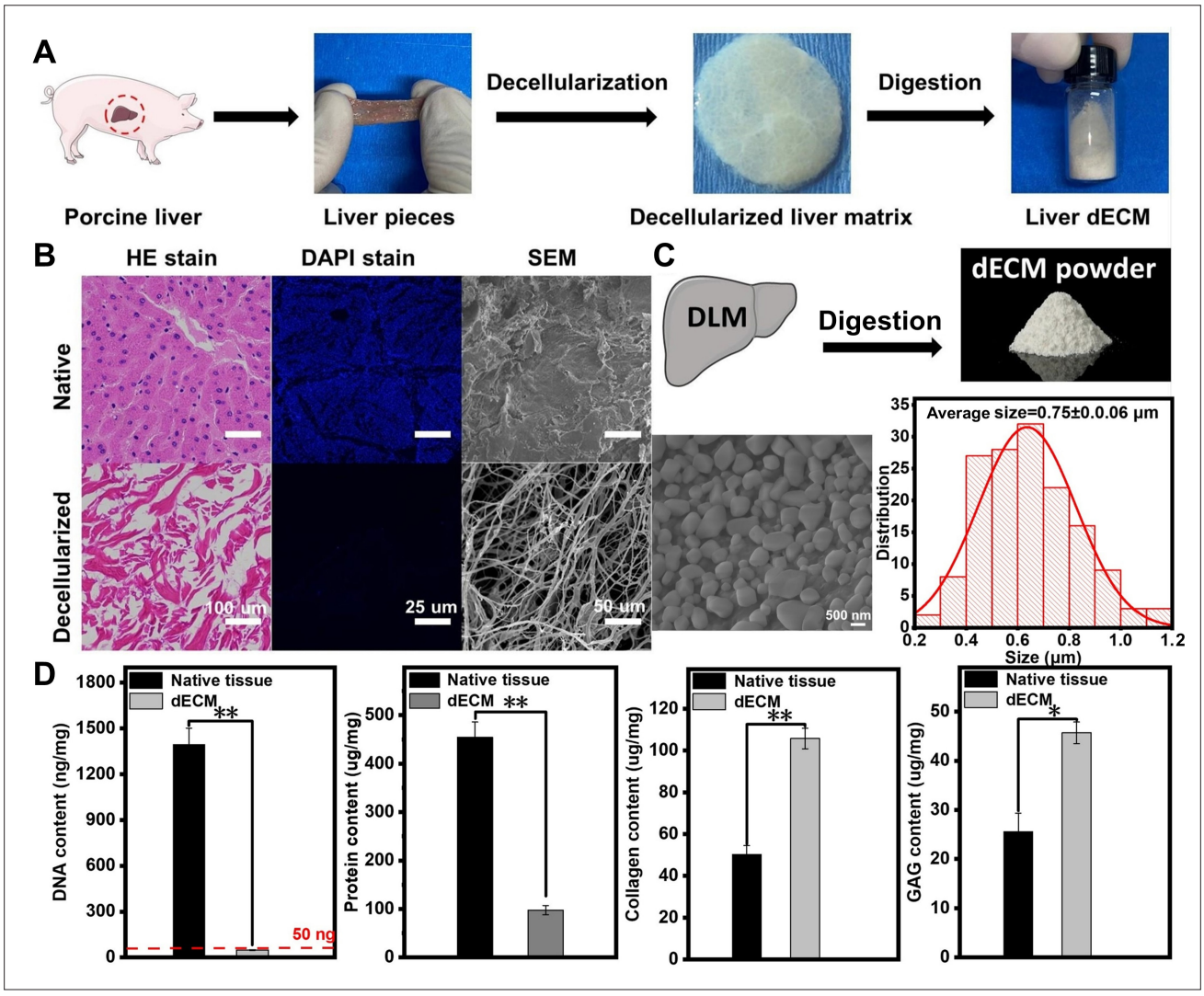

Figure 1. Determination of liver decellularization. (A) The process of decellularized extracellular matrix (dECM) preparation. (B) Hematoxylin and eosin (HE) and 4',6-diamidino-2-phenylindole (DAPI) staining, as well as scanning electron microscopy (SEM) images of the decellularized liver matrix (DLM). Scale bars = 100, 25, and 50 μm, respectively; magnification = 40×, 160×, and 80×, respectively. (C) Morphology of dECM powder. Scale bar = 500 nm; Magnification = 12,000×. (D) Content of biological components ($n = 3$; * $p < 0.05$, ** $p < 0.01$). Abbreviation: GAG, glycosaminoglycan.

to below 50 ng/mg, meeting safety standards for other tissue-derived materials.[46]

The proton nuclear magnetic resonance, FTIR, and the thermogravimetric curves results of gelatin and GelMA are shown in Figure S1, Supporting Information. Protein content significantly decreased after decellularization, while substantial amounts of GAGs and collagen remained, indicating the favorable biological properties of the dECM (collagen I and III staining are shown in Figure S2, Supporting Information). Our previous study reported the proteomic analysis of liver-derived dECM, identifying "catalytic activity" and "cellular process" as the top-ranked molecular function and biological process, respectively.[47] Furthermore, cell viability assays and live/dead staining were performed to assess the impact of decellularization on the cell compatibility of native liver tissue. As shown in Figure S3, Supporting Information, the extract from native liver tissue exhibited significant cytotoxicity, inhibiting cell proliferation, and inducing extensive cell death. In contrast, the DLM group demonstrated normal cell proliferation, nearly matching that of the blank group.

3.2. Hydrogel preparation and characterization

Scanning electron microscopy was applied to inspect the internal morphology of five hydrogels. As shown in Figure 2A, all groups exhibited a macroporous structure (pore size > 50 nm), with average pore sizes of 72.40, 62.74, 43.34, 36.51, and 30.02 μm (Figure 2B). The average pore sizes were 72.40 μm for GM and 62.74 μm for GM/G without dECM. Upon the addition of dECM, the pore size decreased to below 50 μm, with smaller pore sizes corresponding to higher dECM content. These findings suggest that the incorporation of dECM reduces pore size and effectively enhances the compactness of the structure. In addition, dECM particles were visible in the SEM images of dECM-containing groups, appearing as dense and irregular inclusions within the hydrogel network, further confirming their successful integration into the scaffold.

Rheological properties play a crucial role in studying the structure and characteristics of hydrogels, providing valuable guidance for parameter settings in 3D printing. Figure 2C displays the shear viscosity measurements of the printing bioinks at room temperature. It was observed that as the shear rate increased, the viscosity of the bioinks gradually decreased, demonstrating shear-thinning behavior, which is desirable for extrusion-based 3D printing applications.[48] Furthermore, the viscosity increased with rising dECM content, primarily attributed to the higher solid content in the mixture. This viscosity trend also held true for temperature-dependent measurements, as shown in Figure 2D. *G*' and *G*" were utilized to describe the elastic and viscous responses of hydrogels, respectively. As depicted in Figure 2E, as the temperature continuously decreased, the *G*' value initially exceeded the *G*" value, indicating a more dominant elastic behavior. However, a reversal occurred as the temperature approached a certain point. Specifically, the *G*" value of GM/G/d-5 started to increase and eventually surpassed the *G*' value around 24.5°C, indicating a gradual transition from a solid to a liquid state. Among the bioink formulations, GM exhibited the lowest solid–liquid transition temperature, occurring at approximately 15°C. The addition of gelatin increased the solid–liquid transition temperature of the mixture, leading to variations in the transition behavior. The diversity observed among the composite dECM groups could be attributed to differences in dECM content, where a higher proportion of dECM resulted in a higher solid content within the mixture, leading to a more pronounced *G*' value and a delayed transition from solid to liquid state.

3.3. Printing and characterization of gelatin methacrylate/decellularized extracellular matrix bioink three-dimensional scaffold

For the fabrication of printed constructs, the bioinks were extruded from the printer nozzle and stacked to achieve the desired shape. Subsequently, ultraviolet irradiation was applied to induce photo-crosslinking and ensure the curing of the hydrogels (Figure S6). To assess the accuracy of the printed shapes, hydrogels were printed in single-layer grids, featuring square voids between the filaments. The perimeter and area of these void spaces were calculated to determine a printability parameter, Pr. A Pr value of 1 corresponds to a perfect square shape, while values <1 indicate a more circular shape, and values >1 suggest the presence of jagged edges. In our study, all three bioink blends demonstrated Pr values close to 1: GM/G/d-5 = 0.914 ± 0.007, GM/G/d-3 = 0.879 ± 0.04, and GM/G/d-1 = 0.857 ± 0.020, all of which were higher than that of GM/G (0.803 ± 0.022). Notably, pure GelMA could not be successfully printed under these specific printing conditions, highlighting the ideal printability achieved with the developed bioink formulations (Figure 3A). Furthermore, SEM images revealed a more distinct grid structure, indicating superior printability for the GM/G/d-5 bioink compared to other blends, as shown in Figure 3B. To more robustly verify printability beyond simple lattice patterns, complex geometries were also printed using GM/G/d-5, including stylized "HQU" letters, a six-pointed star, and a biomimetic flower-like mesh. As shown in Figure S7, Supporting Information, these shapes maintained sharp edges and fine lattice features, demonstrating the bioink's fidelity under challenging design conditions.

Figure 3C illustrates the swelling properties of the five scaffolds after being immersed in PBS for 12 h. The GM

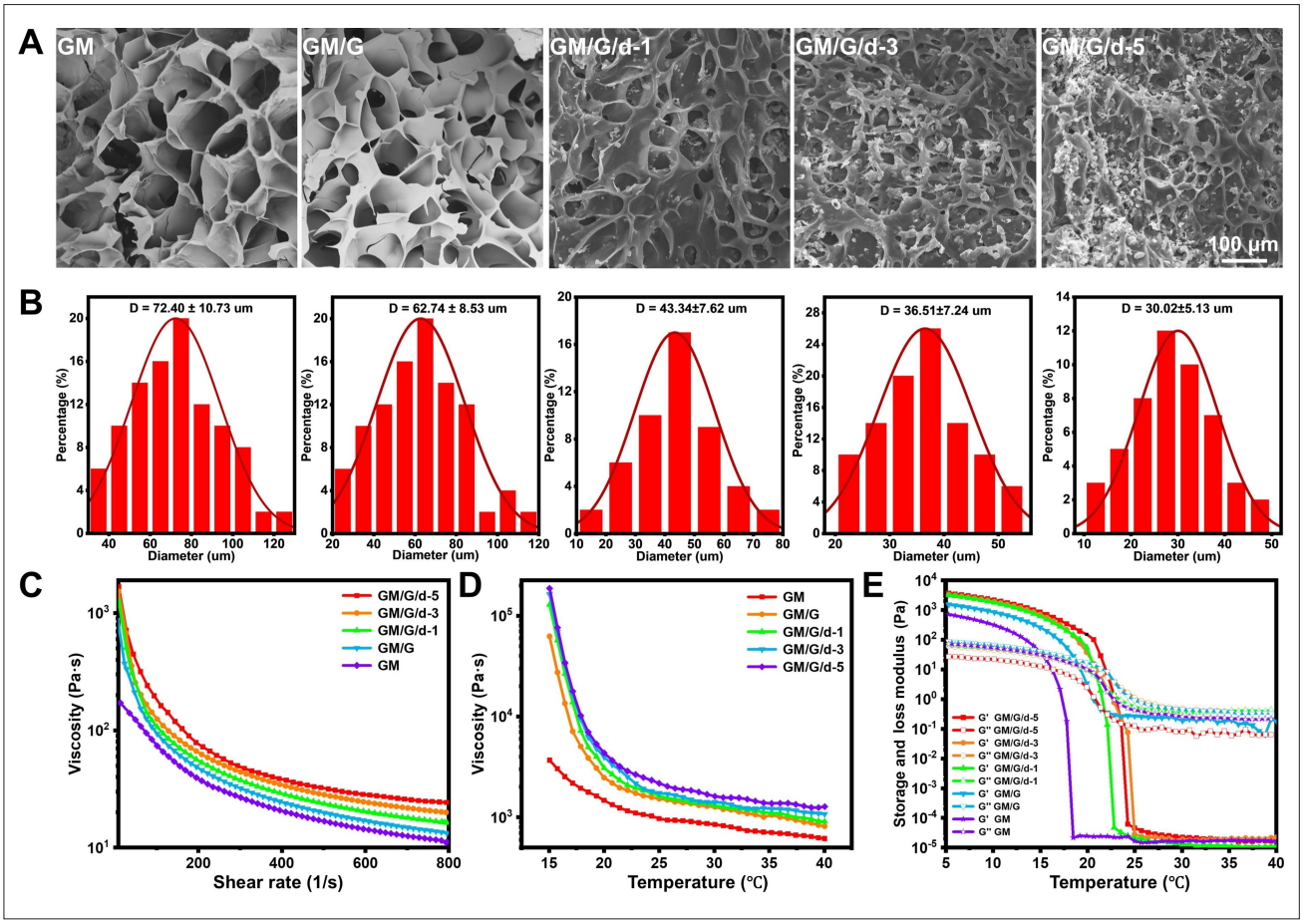

Figure 2. Hydrogel preparation and characterization. (A) Scanning electron microscopy images of five different hydrogels. Scale bar: 100 μm; magnification = 100×. (B) Distribution of macroporous structure diameter of five different hydrogels. (C) Shear rate-dependent viscosity, (D) shear rate-dependent temperature, and (E) viscosity-dependent temperature of different biomaterial ink formulations. Notes: GM: 10% (w/v) gelatin methacrylate (GelMA); GM/G: 10% (w/v) GelMA and 5% (w/v) gelatin; GM/G/d-1, GM/G/d-3, and GM/G/d-5: GM/G combined with decellularized extracellular matrix at concentrations of 1%, 3%, and 5% (w/v), respectively.

scaffold exhibited an Sr of 8.92 within this period, while the GM/G scaffold showed an Sr of 8.05. The scaffolds containing 1%, 3%, and 5% dECM composites exhibited Srs of 7.49, 7.01, and 6.13, respectively. These results indicate that the addition of gelatin and dECM reduced the water absorption capacity due to the higher solid content in the hydrogel, resulting in smaller pore sizes. In contrast, the pure GelMA hydrogel exhibited larger pores, leading to a faster equilibrium rate of swelling and a higher water absorption capacity. Figure 3D presents the *in vitro* degradation properties of the different composite scaffolds. The degradation curves demonstrate that all scaffolds exhibited relatively fast degradation. This could be attributed to the disruption of the physical cross-linking structure of gelatin, as well as the reduced degree of cross-linking caused by the high content of dECM. Over the 9-day experimental observation period, the GM scaffold showed the slowest degradation rate at 14.52 ± 1.03%. In contrast, the GM/G/d-5 group exhibited the fastest degradation rate at 39.74 ± 4.03%. The degradation rates for GM/G, GM/G/d-1, and GM/G/d-3 were measured at 19.9 ± 2.39%, 23.85 ± 2.67%, and 32.14 ± 3.01%, respectively.

Biocompatibility is an essential property of scaffold materials, and L929 cells were applied for scaffold cytotoxicity testing. As shown in Figure 3E, L929 cells grew and proliferated normally in the scaffold extract, in which the cell survival rate was above 90% at both 24- and 48-h intervals. Consistent growth was observed whether cells were cultured in the extract or fresh culture medium, and there was no significant difference between groups. As shown in Figure S4, Supporting Information, the live/dead staining of cells at 48 h where the L929 cell growth density was similar within the field of view, and the group with 5%

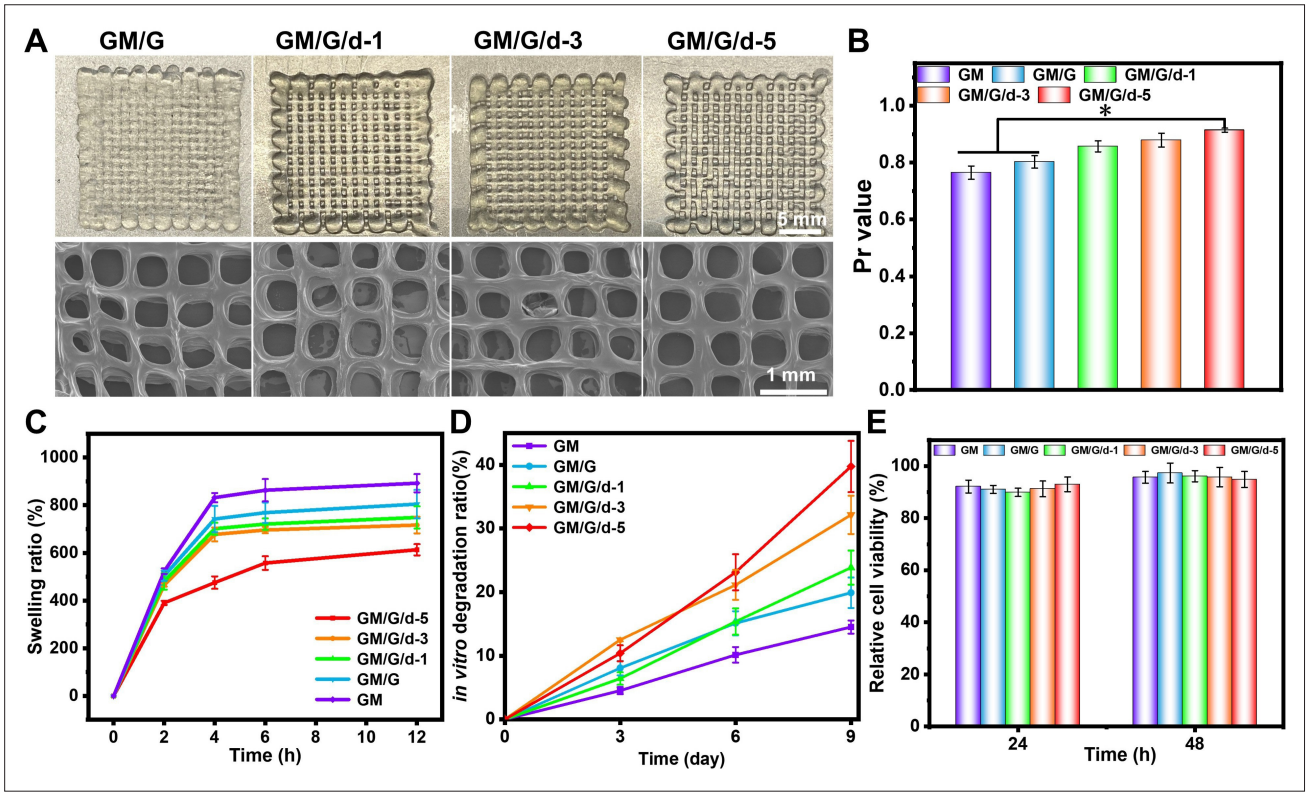

Figure 3. Three-dimensional printing of different scaffolds using five different bioinks and characterizations. (A) Images of scaffolds for each hydrogel. Scale bars: 5 and 1 mm; magnifications = 2.5× and 10×. (B) Printability parameters were calculated as described. Pr = 1 indicates a perfect square. (C) Swelling analysis (n = 3). (D) Degradation analysis (n = 3). (E) Cell viability of five different scaffolds (n = 3). The horizontal lines indicate no significant difference between those groups. * $p < 0.05$. Notes: GM: 10% (w/v) gelatin methacrylate (GelMA); GM/G: 10% (w/v) GelMA and 5% (w/v) gelatin; GM/G/d-1, GM/G/d-3, and GM/G/d-5: GM/G combined with decellularized extracellular matrix at concentrations of 1%, 3%, and 5% (w/v), respectively.

dECM content had relatively more cells. Therefore, the five 3D scaffolds prepared had no apparent cytotoxicity and excellent biocompatibility.

3.4. *In vitro* three-dimensional tumor model construction and assays

Cell migration and growth are fundamental behaviors of tumor cells and tissues.[49] In the CCK-8 assay, hydrogels supplemented with dECM (GM/G/d-1/3/5) demonstrated enhanced cell proliferation compared to the pure GelMA hydrogel, as indicated by higher optical density (OD) values after 3 days (Figure 4A). Additionally, in the scratch wound assay, HepG2 cells cultured with dECM exhibited superior migration capacity compared to those cultured on GM/G and pure GelMA hydrogels (Figure 4B) at 48 h. Figure 4C shows that at 12 h post-scratching, hydrogel solutions containing dECM display enhanced cell migration, with a larger cell migration area than GM and GM/G. By the 48-h mark, the scratch was almost completely healed in the group containing 5% dECM. Considering the overall interaction between each bioink and HepG2 cells, we selected the GM/G/d-5 bioink composition to construct the subsequent 3D *in vitro* tumor model.

3.5. Cell viability and protein expression

To evaluate cell proliferation in the 3D tumor model and 2D culture, CCK-8 and live/dead staining assays were utilized to analyze cell proliferation activity on days 2, 4, 6, and 8. The OD value on day 2 was used as the baseline, and the OD values on days 4, 6, and 8 were normalized accordingly. Fluorescent staining images of live and dead cells under 2D and 3D culture conditions are presented in Figure 5A. Under 2D culture conditions, characterized by rapid cell proliferation, the cells exhibited healthy growth, with only a few dead cells observed. By day 8, the cells had nearly completely covered the surface of the culture plate. Under 3D culture conditions, cells initially grew as individual cells during the first 2 days without aggregation. However, cell spheroids were observed on day 4, and the number and size of cell spheroids significantly increased on days 6 and 8, indicating cell aggregation and growth in a 3D environment with the potential to

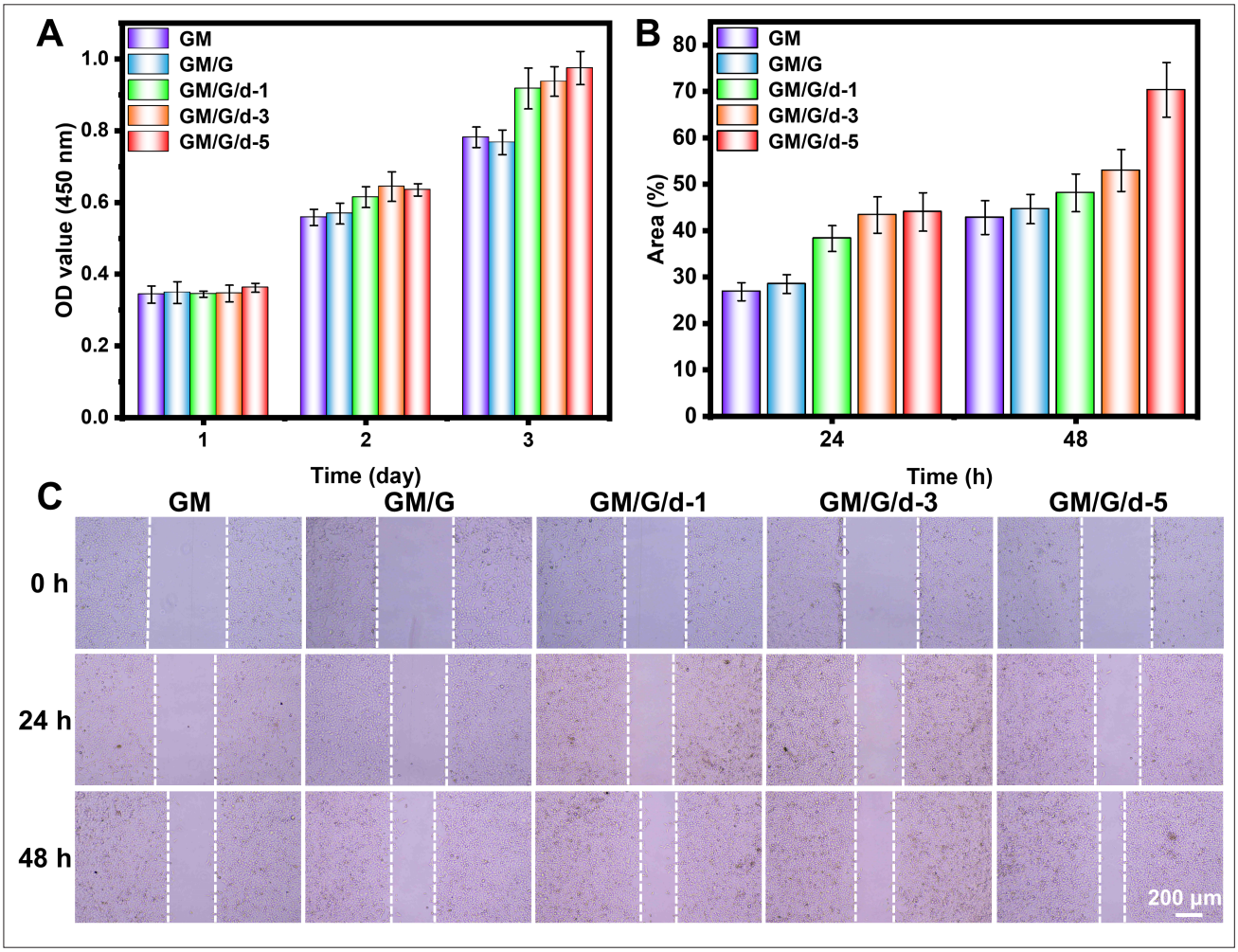

Figure 4. *In vitro* three-dimensional tumor model construction. (A) Cell viability of five different hydrogels encapsulated human hepatocellular carcinoma (HepG2) cells ($n = 3$). (B) Quantification of the migration area ($n = 3$). (C) Cell migration of HepG2 cells in different hydrogel precursor solutions. Scale bar = 200 μm; magnification = 20×. Notes: GM: 10% (w/v) gelatin methacrylate (GelMA); GM/G: 10% (w/v) GelMA and 5% (w/v) gelatin; GM/G/d-1, GM/G/d-3, and GM/G/d-5: GM/G combined with decellularized extracellular matrix at concentrations of 1%, 3%, and 5% (w/v), respectively. Abbreviation: OD, optical density.

develop into microspheres or tissues *in vitro*. As depicted in Figure 5B, under 2D culture conditions, HepG2 cells exhibited proliferation rates of 5.17, 8.77, and 10.17 times on days 4, 6, and 8, respectively, compared to day 2. In contrast, under 3D-dECM culture conditions, HepG2 cells displayed proliferation rates of 5.96, 10.44, and 15.44 times on days 4, 6, and 8, compared to day 2. Under 3D control culture conditions, the corresponding rates were 5.14, 8.99, and 13.78 times. A significant difference in cell proliferation activity was observed on day 4, with a highly significant difference by day 8, indicating enhanced cell proliferation under 3D culture conditions. While cell proliferation in 2D culture was inhibited upon covering the entire surface of the culture plate, the 3D culture provided an additional dimension for cell growth, allowing continuous proliferation. The addition of dECM provided cells with ECM components which could significantly enhance the metabolic activity of cells. Furthermore, the levels of cell protein secretion increased with cultivation time under both 2D and 3D cultures, as demonstrated in Figure 5C. Under 2D culture, protein expression levels were 1.51, 2.37, and 3.58 times higher on days 4, 6, and 8, respectively, compared to day 2. Under 3D culture, protein expression levels were 1.89, 3.34, and 4.75 times higher on days 4, 6, and 8, respectively, compared to day 2. Significant differences in protein secretion levels between 2D and 3D cultures were observed on days 2 and 4, and by day 8, the disparity between the 3D and 2D culture groups became even more pronounced. However, the total protein expression of the 3D control group without dECM was lower than that

of the experimental group, which was consistent with the cell proliferation activity. Together, the data showed that 3D-dECM *in vitro* model had better maintenance of tumor metabolic activity when dECM was supplemented. We propose that the dECM/GelMA bioink-constructed *in vitro* 3D tumor model facilitates cell–ECM interactions and provides adequate space for cellular growth.

3.6. Cellular morphological changes and liver function expression

As depicted in Figure 6A, cells grown under 2D culture conditions exhibited adherent growth to the surface with plump morphology and rapid proliferation. In contrast, under 3D culture conditions, the cells gradually aggregated and formed cell spheres. The addition of 5% dECM during the spheroid formation accelerated cell growth, with numerous aggregates forming on day 4 and larger sphere sizes observed. On day 6 of cultivation, numerous cell spheroids were evident in the 3D-dECM group (marked by red circles), while the 3D control group showed only a few (marked by red arrows). By day 8, both groups exhibited abundant cell spheroids under 3D culture conditions (marked by red circles), with the 3D-dECM group demonstrating greater spheroid size and quantity. By measuring the size of the cell spheroids, it was determined that the average diameters of the 3D control group on days 6 and 8 were 46.64 ± 6.38 and 54.37 ± 9.72 μm, respectively, whereas those of the 3D-dECM group were 67.41 ± 7.3 and 78.83 ± 9.41 μm, respectively (Figure S5, Supporting Information). Under 2D culture conditions, the cells grew as a monolayer without aggregation into cell spheres. Thus, the inclusion of dECM promoted the growth of cell spheres and facilitated the formation of larger cell spheres. These findings align with the results obtained from the co-cultivation of cell materials and scratch experiments discussed in **Section 3.4**, where the presence of 5% dECM demonstrated enhanced interaction with cells, leading to significant improvements in the growth, proliferation, and migration of HepG2 cells.

Liver function markers, such as ALT, AST, ALB, and TBA, were significantly improved in the 3D microenvironment, indicating a positive effect on liver injury and pathological markers of liver cancer cells.[50] The culture supernatants from three groups (2D, 3D control, and 3D-dECM) were analyzed, and the results were normalized to the 2D group to allow comparative evaluation of liver-specific protein expression. Figures 6B–D and S8, Supporting Information illustrate the

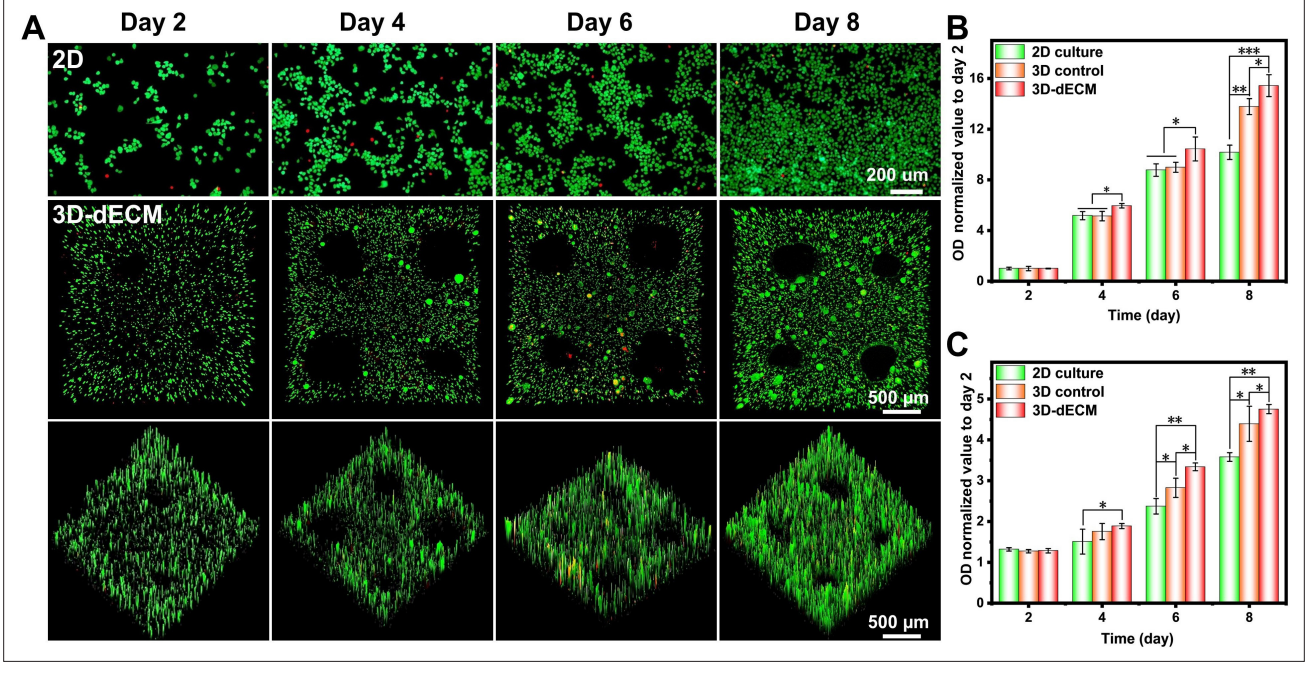

Figure 5. Cell viability and protein expression. (A) Representative live/dead fluorescence images of human hepatocellular carcinoma (HepG2) cells under two-dimensional (2D) and three-dimensional (3D) cultures on days 2, 4, 6, and 8. Scale bars: 200 and 500 μm; magnifications = 20× and 10×. (B) Cell proliferation of HepG2 cells under 2D and 3D culture from day 2 to day 8 ($n = 3$). (C) Total protein of HepG2 cells under 2D and 3D culture from day 2 until day 8 ($n = 3$). The horizontal lines indicate no significant difference between those groups. *$p < 0.05$, **$p < 0.01$, ***$p < 0.001$. Abbreviations: dECM, decellularized extracellular matrix; OD, optical density.

changes in these markers. The expression of pathological markers was higher in the 3D culture group compared to the 2D group. After 8 days of culture, the levels of ALT, AST, and TBA in the 3D-dECM group were 3.26 ± 0.47, 1.73 ± 0.21, and 2.01 ± 0.24 times higher, respectively, compared to the 2D culture conditions. The 3D control group exhibited significantly higher ALB secretion than the 2D group ($p < 0.001$), while the 3D-dECM group showed further enhancement ($p < 0.05$) relative to the 3D control, indicating that the inclusion of liver-derived dECM further promoted hepatic functionality. Moreover, the group treated with added dECM showed higher expression levels of these markers compared to the group without dECM treatment, suggesting that the 3D culture tumor model more closely resembles an *in vivo* solid tumor.

3.7. Chemoresistance

To assess the drug toxicity of PTX and DOX on tumor cells in different culture conditions and drug concentrations, both drugs were introduced to 2D and 3D tumor models, followed by a 24-h incubation period. Figure 7A and B illustrates the distinct effects of drug treatment in 2D and 3D culture environments. In 2D cultures, a substantial

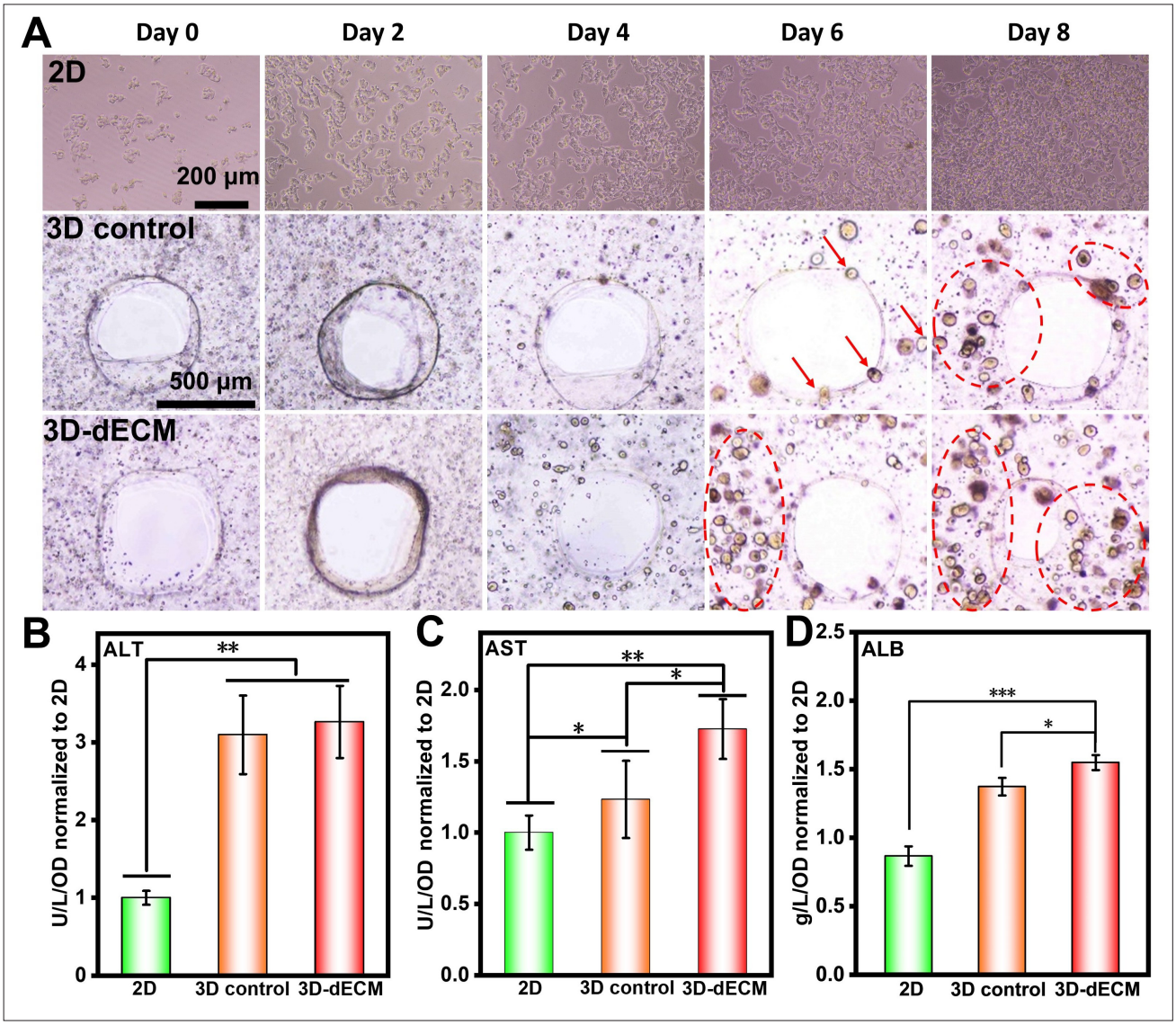

Figure 6. Cellular morphological change and liver function expression. (A) Cell morphology under different culture conditions: two-dimensional (2D) culture, the three-dimensional (3D) control group, and 3D-decellularized extracellular matrix (dECM). Scale bars: 200 and 500 μm; magnifications = 20× and 10×. Liver function indexes: (B) ALT, (C) AST, and (D) ALB ($n = 3$). (The horizontal lines indicate no significant difference between those groups. *$p < 0.05$, **$p < 0.01$). Abbreviations: ALB, albumin; ALT, alanine aminotransferase; AST, aspartate aminotransferase; OD, optical density.

number of cells exhibited red staining, indicating cell death, while only a small fraction remained viable. In contrast, within 3D cultures, limited cell death was observed after 12 h, primarily among cells that had not formed spheroids. By the 24-h mark, most of these non-spheroid cells had succumbed to treatment. However, the spheroids predominantly displayed green staining, with only a few showing red staining. These results highlight the enhanced drug resistance of cell spheroids, which is consistent with findings from previous studies. Cell viability and staining were assessed at 12- and 24-h time points, respectively. As shown in Figure 7C and D, under 2D culture conditions, treatment with DOX resulted in cell survival rates of 36.23% and 18.88% at a drug concentration of 100 μg/mL after 12 and 24 h, respectively. For PTX, the survival rates were 21.04% and 14.04% under the same conditions and time points. In contrast, within the 3D-dECM culture group, the survival rate for cells treated with DOX was 46.23% after 12 h and 31.34% after 24 h, at a drug concentration of 100 μg/mL. Similarly, following treatment with PTX, the survival rate was 41.36% at 12 h and 34.72% at 24 h. These findings suggest that cells exhibited greater drug resistance in 3D culture conditions. This resistance can be attributed to the enhanced survival mechanisms of cell spheroids, which form through cellular aggregation, as well as reduced drug penetration and uptake within the spheroid structure. hrough UV-Vis spectroscopic analysis, it was further revealed that significantly lower doxorubicin uptake was detected in 3D-dECM constructs compared to 2D cultures, indicative of limited drug penetration due to the hydrogel matrix and spheroidal structure (Figure S9). Specifically, it has been reported that 3D culture alone can

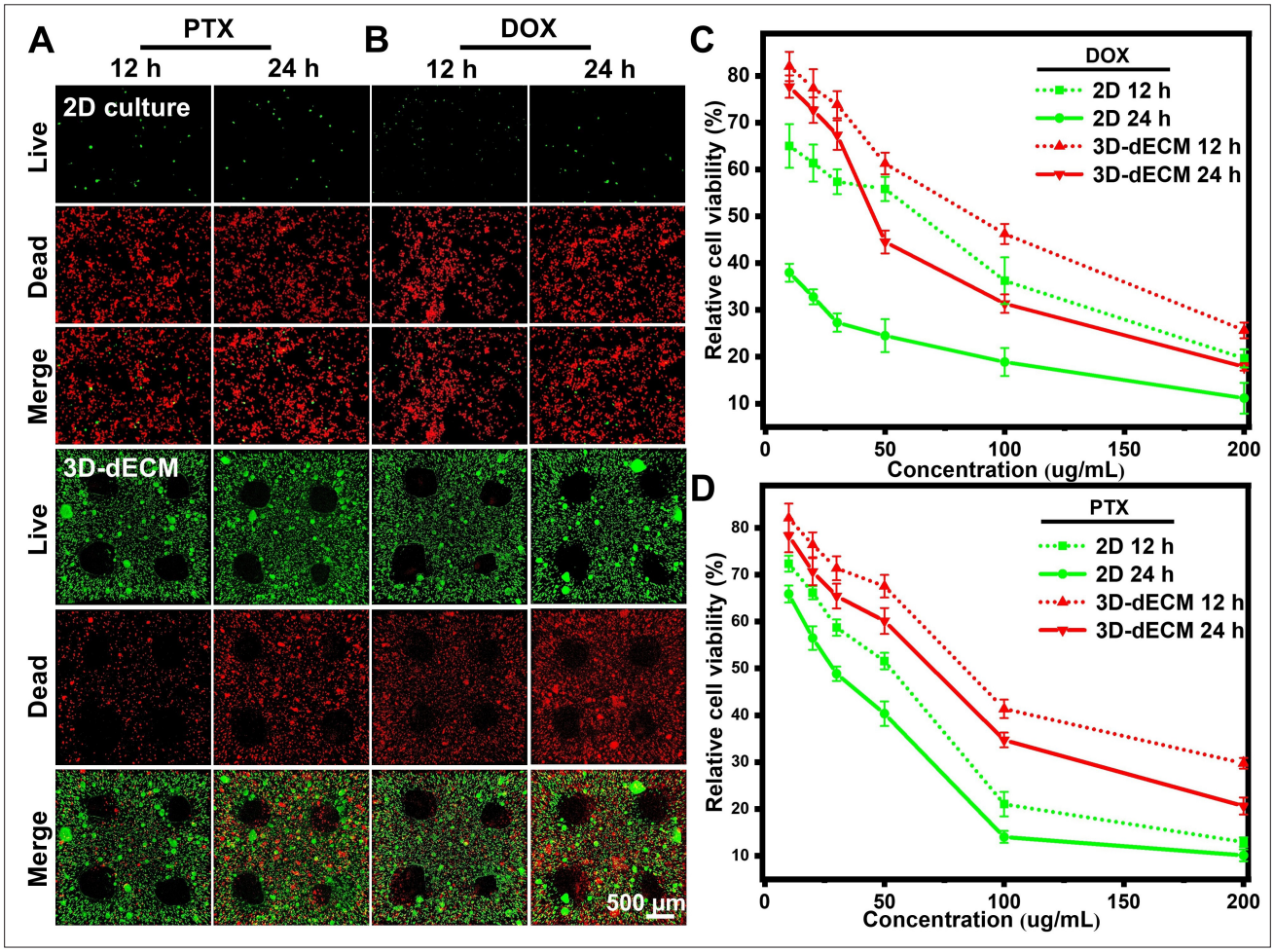

Figure 7. Chemoresistance of human hepatocellular carcinoma (HepG2) cells cultured in three-dimensional (3D)-decellularized extracellular matrix (dECM) constructs compared to two-dimensional (2D) planar culture. Live/dead staining of HepG2 cells in 3D-dECM constructs and 2D culture after (A) PTX and (B) DOX treatment at 12 and 24 h. Scale bar: 500 μm; magnification = 20× and 10×. Relative cell viability after (C) DOX and (D) PTX at 12 and 24 h (n = 3). Abbreviations: DOX, doxorubicin; PTX, paclitaxel.

promote hepatocyte-like phenotypes through improved cell–cell and cell–matrix interactions.[51] Furthermore, the use of maintenance medium[52] and galactosylated substrates that mimic liver-specific glycosylation patterns[53] can further enhance hepatic gene expression, protein secretion, and metabolic functions *in vitro*. These functional enhancements may increase the cellular capacity for drug detoxification, efflux transporter activity, or resistance to apoptosis, thereby contributing to the chemoresistant phenotype observed in 3D tumor models.

4. Conclusion

This study implemented an integrated approach that combines chemical decellularization with enzymatic treatment to optimize the preparation conditions for dECM. Comprehensive assessments of the physicochemical properties and biocompatibility of dECM confirmed its safety and effectiveness. To address the inherent limitations of dECM in printability, composite bioinks consisting of GelMA, gelatin, and dECM were formulated and systematically analyzed. Rheological assessments, structural imaging, and extended shape printing demonstrated that the incorporation of dECM not only enhanced the mechanical integrity and structural fidelity of the bioinks, but also maintained excellent biocompatibility. Furthermore, an *in vitro* 3D liver cancer model was developed using GelMA, gelatin, and dECM, enabling a comprehensive investigation of tumor growth dynamics, metabolic activity, protein secretion, and drug resistance. The findings underscore that 3D printing technology serves as an effective methodology for constructing *in vitro* tumor models, with dECM significantly promoting cell proliferation, migration, and aggregation. Notably, the liver cancer model developed through this innovative approach demonstrated significantly enhanced cell proliferation, protein expression, and drug resistance compared to conventional 2D culture systems. This model not only provides critical insights into tumor biology but also presents a robust platform for the screening of novel targeted therapies, thereby paving the way for advancements in cancer research and treatment.

Acknowledgments

The authors thank the Instrumental Analysis Center of Huaqiao University for their FT-IR, NMR, SEM, and CLSM measurement support.

Funding

This work was supported by the National Natural Science Foundation of China (NSFC, 32271410 and 32071323, and 32301117), the Natural Science Foundation of Fujian Province (No. 2022J01297), the Fundamental Research Funds for the Central Universities (ZQN-1107), and the Science and Technology Projects in Fujian Province (2022FX1 and 2023Y4008).

Conflict of interest

The authors declare that they have no known competing financial interests or personal relationships that could have appeared to influence the work reported in this paper.

Author contributions

Conceptualization: Chunyang Zhang, Chaoping Fu
Formal analysis: Chunyang Zhang, Chaoping Fu
Funding acquisition: Shibin Wang, Aizheng Chen, Chaoping Fu
Investigation: Chunyang Zhang, Yunze Xu, Xiaochang Lu
Methodology: Chunyang Zhang, Yunze Xu, Hongwei Yu
Project administration: Shibin Wang, Aizheng Chen, Chaoping Fu
Supervision: Chaoping Fu
Visualization: Chunyang Zhang, Ying Fang, Hongwei Yu
Writing–original draft: Chunyang Zhang
Writing–review & editing: Changyong Li, Weihong Ji, Chaoping Fu

Ethics approval and consent to participate

Not applicable.

Consent for publication

Not applicable.

Availability of data

Additional data and materials not included in the manuscript or supplementary materials are available from the corresponding authors upon reasonable request.

References

1. De Santibañes M, Pekolj J, Sanchez Claria R, De Santibañes E, Mazza OM. Technical implications for surgical resection in locally advanced pancreatic cancer. *Cancers*. 2023;15(5):1509.
doi: 10.3390/cancers15051509

2. Zaher A, Foromera J, Capanu M, Chou J, Faleck DM. Sa1848 extent of surgical resection for ibd-associated neoplasia and colorectal cancer outcomes. *Gastroenterology*. 2024;166(5):S-549-S-550.
doi: 10.1016/S0016-5085(24)01733-5

3. Yu X, Wang X, Sun L, Yamazaki A, Li X. Tumor microenvironment regulation - enhanced radio - immunotherapy. *Biomater Adv*. 2022;138:212867.
doi: 10.1016/j.bioadv.2022.212867

4. Pan S, Sun Z, Zhao B, et al. Therapeutic application of manganese-based nanosystems in cancer radiotherapy. *Biomaterials*. 2023;302:122321. doi: 10.1016/j.biomaterials.2023.122321

5. Moy B, Rumble RB, Carey LA, for the Chemotherapy and Targeted Therapy for Endocrine-Pretreated or Hormone Receptor–Negative Metastatic Breast Cancer Expert Panel. Chemotherapy and targeted therapy for endocrine-pretreated or hormone receptor–negative metastatic breast cancer: ASCO guideline rapid recommendation update. *JCO*. 2023;41(6):1318-1320. doi: 10.1200/JCO.22.02807

6. Garg V, Kumar L. Metronomic chemotherapy in ovarian cancer. *Cancer Lett*. 2023;579:216469. doi: 10.1016/j.canlet.2023.216469

7. Michalczyk K, Pawlik J, Czekawy I, Kozłowski M, Cymbaluk-Płoska A. Complementary methods in cancer treatment—cure or curse? *IJERPH*. 2021;18(1):356. doi: 10.3390/ijerph18010356

8. Li Y, Xu X. Nanomedicine solutions to intricate physiological-pathological barriers and molecular mechanisms of tumor multidrug resistance. *J Control Release*. 2020;323:483-501. doi: 10.1016/j.jconrel.2020.05.007

9. Mao S, He J, Zhao Y, et al. Bioprinting of patient-derived *in vitro* intrahepatic cholangiocarcinoma tumor model: establishment, evaluation and anti-cancer drug testing. *Biofabrication*. 2020;12(4):045014. doi: 10.1088/1758-5090/aba0c3

10. Xu X, Liu Y, Liu Y, et al. Functional hydrogels for hepatocellular carcinoma: Therapy, imaging, and in vitro model. *J Nanobiotechnol*. 2024;22(1):381. doi: 10.1186/s12951-024-02547-9

11. Li W, Hu X, Yang S, et al. A novel tissue-engineered 3D tumor model for anti-cancer drug discovery. *Biofabrication*. 2018;11(1):015004. doi: 10.1088/1758-5090/aae270

12. Vitale S, Calapà F, Colonna F, et al. Advancements in 3D in vitro models for colorectal cancer. *Adv Sci*. 2024;11(32):2405084. doi: 10.1002/advs.202405084

13. Lv J, Du X, Wang M, Su J, Wei Y, Xu C. Construction of tumor organoids and their application to cancer research and therapy. *Theranostics*. 2024;14(3):1101-1125. doi: 10.7150/thno.91362

14. Van Tienderen GS, Conboy J, Muntz I, et al. Tumor decellularization reveals proteomic and mechanical characteristics of the extracellular matrix of primary liver cancer. *Biomater Adv*. 2023;146:213289. doi: 10.1016/j.bioadv.2023.213289

15. Krujatz F, Dani S, Windisch J, et al. Think outside the box: 3D bioprinting concepts for biotechnological applications – recent developments and future perspectives. *Biotechnol Adv*. 2022;58:107930. doi: 10.1016/j.biotechadv.2022.107930

16. Levato R, Dudaryeva O, Garciamendez-Mijares CE, et al. Light-based vat-polymerization bioprinting. *Nat Rev Methods Primers*. 2023;3(1):47. doi: 10.1038/s43586-023-00231-0

17. Kumar S, Tharayil A, Thomas S. 3D bioprinting of nature-inspired hydrogel inks based on synthetic polymers. *ACS Appl Polym Mater*. 2021;3(8):3685-3701. doi: 10.1021/acsapm.1c00567

18. Yang K, Wang L, Vijayavenkataraman S, Yuan Y, Tan ECK, Kang L. Recent applications of three-dimensional bioprinting in drug discovery and development. *Adv Drug Deliv Rev*. 2024;214:115456. doi: 10.1016/j.addr.2024.115456

19. Bian S, Hu X, Zhu H, et al. 3D bioprinting of artificial skin substitute with improved mechanical property and regulated cell behavior through integrating patterned nanofibrous films. *ACS Nano*. 2024;18(28):18503-18521. doi: 10.1021/acsnano.4c04088

20. Kronemberger GS, Spagnuolo FD, Karam AS, Chattahy K, Storey KJ, Kelly DJ. Rapidly degrading hydrogels to support biofabrication and 3D bioprinting using cartilage microtissues. *ACS Biomater Sci Eng*. 2024;10(10):6441-6450. doi: 10.1021/acsbiomaterials.4c00819

21. Pérez Del Río E, Rey-Vinolas S, Santos F, et al. 3D printing as a strategy to scale-up biohybrid hydrogels for T cell manufacture. *ACS Appl Mater Interfaces*. 2024;16(38):50139-50146. doi: 10.1021/acsami.4c06183

22. Pramanick A, Hayes T, Sergis V, McEvoy E, Pandit A, Daly AC. 4D bioprinting shape-morphing tissues in granular support hydrogels: Sculpting structure and guiding maturation. *Adv Funct Mater*. 2025;35(5):2414559. doi: 10.1002/adfm.202414559

23. Patel ZH, Charania AA, Punjani Z, et al. Evaluating anticancer agents on 3D bioprinted organoid tumors (BOT) to reduce cost and accelerate therapeutic discovery. *JCO*. 2022;40(16_suppl):e13500. doi: 10.1200/JCO.2022.40.16_suppl.e13500

24. Kankala RK, Zhang YS, Kang L, Ambrosio L. Editorial: Polymeric microarchitectures for tissue regeneration and drug screening. *Front Bioeng Biotechnol*. 2023;11:1144991. doi: 10.3389/fbioe.2023.1144991

25. Wang Y, Jeon H. 3D cell cultures toward quantitative high-throughput drug screening. *Trends Pharmacol Sci*. 2022;43(7):569-581. doi: 10.1016/j.tips.2022.03.014

26. González-Callejo P, García-Astrain C, Herrero-Ruiz A, et al. 3D bioprinted tumor-stroma models of triple-negative breast cancer stem cells for preclinical targeted therapy evaluation. *ACS Appl Mater Interfaces*. 2024;16(21):27151-27163. doi: 10.1021/acsami.4c04135

27. Ferreira LP, Gaspar VM, Mano JF. Decellularized extracellular matrix for bioengineering physiomimetic 3D in vitro tumor models. *Trends Biotechnol*. 2020;38(12):1397-1414. doi: 10.1016/j.tibtech.2020.04.006

28. García-Astrain C, Henriksen-Lacey M, Lenzi E, et al. A scaffold-assisted 3D cancer cell model for surface-enhanced Raman scattering-based real-time sensing and imaging. *ACS Nano*. 2024;18(17):11257-11269. doi: 10.1021/acsnano.4c00543

29. Ebrahimighaei R, Tarassova N, Bond SC, et al. Extracellular matrix stiffness controls cardiac fibroblast proliferation via the nuclear factor-Y (NF-Y) transcription factor. *Biochim Biophys Acta Mol Cell Res*. 2024;1871(2):119640. doi: 10.1016/j.bbamcr.2023.119640

30. Fu Y, Zhou Y, Wang K, Li Z, Kong W. Extracellular matrix interactome in modulating vascular homeostasis and remodeling. *Circ Res*. 2024;134(7):931-949. doi: 10.1161/CIRCRESAHA.123.324055

31. Guo WY, Wang WH, Xu PY, Kankala RK. Decellularised extracellular matrix-based injectable hydrogels for tissue engineering applications. *Biomater Transl*. 2024;5(2):114-128. doi: 10.12336/biomatertransl.2024.02.003

32. Naba A. Mechanisms of assembly and remodelling of the extracellular matrix. *Nat Rev Mol Cell Biol*. 2024;25(11):865-885. doi: 10.1038/s41580-024-00767-3

33. Zhou Z, Zhang Y, Zeng Y, et al. Effects of nanomaterials on synthesis and degradation of the extracellular matrix. *ACS Nano*. 2024;18(11):7688-7710. doi: 10.1021/acsnano.3c09954

34. Bhar B, Ranta P, Samudrala PK, Mandal BB. Omentum extracellular matrix-silk fibroin hydroscaffold promotes wound healing through vascularization and tissue remodeling in the diabetic rat model. *ACS Biomater Sci Eng*. 2024;10(2):1090-1105. doi: 10.1021/acsbiomaterials.3c01877

35. Tam NW, Becker A, Mangiarotti A, Cipitria A, Dimova R. Extracellular vesicle mobility in collagen I hydrogels is influenced by matrix-binding integrins. *ACS Nano*. 2024;18(43):29585-29601. doi: 10.1021/acsnano.4c07186

36. Puistola P, Kethiri A, Nurminen A, et al. Cornea-specific human adipose stem cell-derived extracellular matrix for corneal stroma tissue engineering. *ACS Appl Mater Interfaces*. 2024;16(13):15761-15772. doi: 10.1021/acsami.3c17803

37. Na J, Yang Z, Shi Q, et al. Extracellular matrix stiffness as an energy metabolism regulator drives osteogenic differentiation in mesenchymal stem cells. *Bioact Mater*. 2024;35:549-563. doi: 10.1016/j.bioactmat.2024.02.003

38. Tao M, Ao T, Mao X, et al. Sterilization and disinfection methods for decellularized matrix materials: review, consideration and proposal. *Bioact Mater*. 2021;6(9):2927-2945. doi: 10.1016/j.bioactmat.2021.02.010

39. Snyder Y, Jana S. Strategies for development of decellularized heart valve scaffolds for tissue engineering. *Biomaterials*. 2022;288:121675. doi: 10.1016/j.biomaterials.2022.121675

40. Lian L, Xie M, Luo Z, et al. Rapid volumetric bioprinting of decellularized extracellular matrix bioinks. *Adv Mater*. 2024;36(34):2304846. doi: 10.1002/adma.202304846

41. Niu R, Xin Q, Xu E, Yao S, Chen M, Liu D. Nanostarch-stimulated cell adhesion in 3D bioprinted hydrogel scaffolds for cell cultured meat. *ACS Appl Mater Interfaces*. 2024;16(18):23015-23026. doi: 10.1021/acsami.4c03585

42. Bae M, Kim JJ, Kim J, Cho DW. Decellularized extracellular matrix for three- dimensional bioprinted in vitro disease modeling. *Int J Bioprint*. 2024;10(2):1970. doi: 10.36922/ijb.1970

43. Shin M, Galarraga JH, Kwon MY, Lee H, Burdick JA. Gallol-derived ECM-mimetic adhesive bioinks exhibiting temporal shear-thinning and stabilization behavior. *Acta Biomater*. 2019;95:165-175. doi: 10.1016/j.actbio.2018.10.028

44. Ouyang L, Yao R, Zhao Y, Sun W. Effect of bioink properties on printability and cell viability for 3D bioplotting of embryonic stem cells. *Biofabrication*. 2016;8(3):035020. doi: 10.1088/1758-5090/8/3/035020

45. Brumberg VA, Bikmulina PY, Pozdnyakov AA, et al. Scaling liver bioprinting: a guide for usage of the hepatic extracellular matrix as a bioink. *Int J Bioprint*. 2025;11(1):57-83. doi: 10.36922/ijb.4343

46. Ouyang L, Yao R, Zhao Y, Sun W. Effect of bioink properties on printability and cell viability for 3D bioplotting of embryonic stem cells. *Biofabrication*. 2016;8(3):035020. doi: 10.1088/1758-5090/8/3/035020

47. Choudhury D, Tun HW, Wang T, Naing MW. Organ-derived decellularized extracellular matrix: a game changer for bioink manufacturing? *Trends Biotechnol*. 2018;36(8):787-805. doi: 10.1016/j.tibtech.2018.03.003

48. Xu P, Kankala RK, Wang S, Chen A. Decellularized extracellular matrix-based composite scaffolds for tissue engineering and regenerative medicine. *Regen Biomater*. 2023;11:rbad107. doi: 10.1093/rb/rbad107

49. Khati V, Ramachandraiah H, Pati F, Svahn HA, Gaudenzi G, Russom A. 3D bioprinting of multi-material decellularized liver matrix hydrogel at physiological temperatures. *Biosensors*. 2022;12(7):521. doi: 10.3390/bios12070521

50. Myojin Y, Hikita H, Sugiyama M, et al. Hepatic stellate cells in hepatocellular carcinoma promote tumor growth via growth differentiation factor 15 production. *Gastroenterology*. 2021;160(5):1741-1754.e16.
doi: 10.1053/j.gastro.2020.12.015

50. Wang Y, Kankala RK, Zhang J, et al. Modeling endothelialized hepatic tumor microtissues for drug screening. *Adv Sci*. 2020;7(21):2002002.
doi: 10.1002/advs.202002002

52. Baharvand H, Hashemi SM, Kazemi Ashtiani S, Farrokhi A. Differentiation of human embryonic stem cells into hepatocytes in 2D and 3D culture systems in vitro. *Int J Dev Biol*. 2006;50(7):645-652.
doi: 10.1387/ijdb.052072hb

53. Krueger WH, Tanasijevic B, Barber V, et al. Cholesterol-secreting and statin-responsive hepatocytes from human ES and iPS cells to model hepatic involvement in cardiovascular health. *PLoS ONE*. 2013;8(7):e67296.
doi: 10.1371/journal.pone.0067296

54. Gevaert E, Billiet T, Declercq H, Dubruel P, Cornelissen R. Galactose-functionalized gelatin hydrogels improve the functionality of encapsulated Hepg2 cells. *Macromol Biosci*. 2014;14(3):419-427.
doi: 10.1002/mabi.201300320